Comparative Electrochemical Charge Storage Properties of Bulk and Nanoscale Vanadium Oxide Electrodes

David McNulty[1], D. Noel Buckley,[2,3] and Colm O'Dwyer[1,4]*

[1] *Department of Chemistry, University College Cork, Cork, T12 YN60, Ireland*
[2] *Department of Physics and Energy, University of Limerick, Limerick, V94 T9PX, Ireland*
[3] *Materials & Surface Science Institute, University of Limerick, Limerick, V94 T9PX, Ireland*
[4] *Micro-Nano Systems Centre, Tyndall National Institute, Lee Maltings, Cork, T12 R5CP, Ireland*

***Contact details:** Tel: +353 (0)21 4902732; Fax: +353 (0)21 4274097; email: c.odwyer@ucc.ie

Abstract

Vanadium oxide nanostructures have been widely researched as a cathode material for Li-ion batteries due to their layered structure and shorter Li^+ diffusion path lengths, compared to the bulk material. Some oxides exhibit charge storage due to capacitive charge compensation and many materials with cation insertion regions and rich surface chemistry have complex responses to lithiation. Herein, detailed analysis of cyclic voltammetry curves was used to distinguish between the charge stored due to lithium intercalation processes, and from extrinsic capacitive effects for micron-scale bulk V_2O_5 and synthesized nano-scale vanadium oxide polycrystalline nanorods (poly-NRs) designed to exhibit multivalent surface oxidation states. The results demonstrate that at fast scan rates (up to 500 mV/s) the contribution due to diffusion-controlled intercalation processes in to micron V_2O_5 and nanoscale V_2O_3 are found to dominate irrespective of size and multivalent surface chemistry. At slow potential scan rates, a greater portion of the redox events are capacitive in nature for the polycrystalline nanorods. Low dimensional vanadium oxide structures of V_2O_5 or V_2O_3, with greater surface area does not automatically increase its (redox) pseudocapacitive behaviour significantly at any scan rate, even with multivalent surface oxidation states.

Introduction

Over the past two decades there has been an intense research effort aimed at identifying nanostructured materials for application as electrode materials for Li-ion batteries with increased safety, energy density, cycle life and lower cost. [1-7] Nanostructured materials have been widely researched for both the cathode and anode, mainly due to their increased surface area, when compared to their bulk counterparts, and shorter Li^+ diffusion lengths due to their nano-scale dimensions [8-14].

In recent years there has also been a tremendous increase in research devoted to investigating materials that may combine the high energy density of batteries and the long cycle life and short charging times of supercapacitors. [15-17] Vanadium oxides represent an attractive candidate as a cathode material due to their layered structure and high theoretical capacity [18-24] in the V_2O_5 structure, but it can also intercalate Li into the V_2O_3 phase. As a result of their layered structure [25-28] it may be assumed that the total stored charge for vanadium oxide nanostructures in Li-ion battery applications is exclusively due to diffusion-based intercalation processes associated with well-defined phase changes in bulk crystalline V_2O_5. However, from cyclic voltammetry analysis over a range of different scan rates it is possible to determine the contribution of diffusion and capacitive effects to the total stored charge [29-33], a charge-compensation effect in metal oxides (even in a Li-ion electrolyte) that is still a matter of debate in the literature. Capacitive effects include the charge transfer process with surface atoms of the host material, referred to as pseudocapacitance [34] and the contribution from the double layer effect [35,29,36]. Note that redox pseudocapacitance versus double layer capacitance behave as either Faradaic or non-Faradaic processes. In metal oxides such as V_2O_5, oxygen vacancies have been suggested as a possible mechanism for surface chemical redox couples to compensate charge with Li^+ without solid state chemical changes in the crystal [37], and 'intercalation' pseudocapacitance is purported to provide a

similar mechanism without layer puckering or volume expansion changes from chemical reaction with the cation [17].

It is important to determine how significant the contribution for both diffusion-based intercalation or alloying reactions versus (any) capacitive effects are on the total stored charge to enable a better understanding of how charge is stored in both cathode and anode materials [15], particularly when size effects are purported to play a significant role. Electrochemical quartz microbalance techniques can fingerprint whether changes in electrode mass are found, thus linking the response to intercalation versus double layer capacitance storage differences [38]. Understanding how material surface chemistry, size and structure can influence the very nature of the electrochemical energy storage mechanisms is critical for new and emerging high performance materials. Apart from mechanism identification, the rate and voltage dependence of pseudocapacitance versus intercalation may offer charge storage options with controllable volumetric changes. Previous pseudocapacitive studies have been reported other Li-ion battery materials such as TiO_2 [31], MnO_2 [39] and MoO_3 [40]. The pseudocapacitive behaviour of vanadium oxide materials has been reported [41,42], but the quantitative assessment of the basis for the charge capacities was not assessed in detail. The pseudocapacitive behaviour of vanadium oxide and other transition metal oxide structures have previously been inferred from the shape of insertion/removal or even redox peaks in cyclic voltammograms. [43,29,44] We quantify the capacitive contributions towards the measured current through a systematic analysis of cyclic voltammograms acquired at a range of different scan rates. The data define the relative contributions of phase, surface chemistry and size on the contributions to intercalation and capacitive processes for vanadium oxide battery electrode materials, and is generally applicable to voltammetric measurements of many other systems.

Here, we detail the formation of vanadium oxide polycrystalline nanorods and compare their response to potentiodynamic polarization to that of bulk-size vanadium pentoxide crystals. We describe detailed analysis of cyclic voltammetric polarization of nanorods with a comparatively richer surface defect chemistry. One significant difference between battery and pseudocapacitive materials is that the cycling of battery materials can be quite slow, whereas the cycling of pseudocapacitive materials can occur in a matter of minutes. [16] Hence, we examined our vanadium oxide samples at slow (0.1 mVs^{-1}) and fast (500 mVs^{-1}) scan rates. X-ray photoelectron spectroscopy, X-ray diffraction and electron microscopy were used to identify differences in surface chemistry and crystal structure, whereby nanorods present multiple vanadium valence states, higher surface area and smaller dimensions. We detail how the total charge stored by vanadium oxide electrode materials is not exclusively due to intercalation based processes but also capacitive processes. The data shows that there is a transition from intercalation-mode reactions to capacitive charge storage at slower scan rates in different potential ranges for nanoscale and bulk vanadium oxide materials. At higher scan rates, intercalation and diffusion-based reaction processes occur at electrode materials on bulk or nanoscale level even with markedly different multivalent surface chemistry. Most importantly, the data shows that nanoscale engineering of multivalent vanadium oxide does not automatically infer a transition to capacitive behaviour in spite of a rich surface chemistry, since the intercalation rate and chemical potentials are preferable to surface region storage.

Experimental

Vanadium oxide nanorods were prepared by annealing vanadium oxide nanotubes (VONTs) as previously reported [45,46]. VONTs were synthesised via hydrothermal treatment of a

vanadium oxide xerogel mixed with nonylamine. The as-prepared VONTs were then annealed to 600 ^{o}C in a nitrogen atmosphere, resulting in a structural transformation from VONTs to vanadium oxide polycrystalline nanorods (poly-NRs). TEM analysis was conducted using a JEOL JEM-2100F TEM operating at 200 kV. SEM analysis was performed using a Hitachi S-4800 at an accelerating voltage of 10 kV. The electrochemical properties of bulk V_2O_5 powder and poly-NRs were investigated using a two electrode, stainless steel split cell. Bulk V_2O_5 and Poly-NR electrodes were prepared using the same method. A suspension of each powder was prepared by sonication in ethanol. Using a micropipette, the suspension was then drop-cast on to 1 cm^2 pieces of stainless steel. Electrodes were allowed to dry in air for 30 minutes to allow the ethanol to evaporate and then heated at 100 ^{o}C for 1 hour to increase adhesion between the active material powder and the stainless steel substrate. No additional conductive additives or binders were added to the various vanadium oxide working electrodes. This electrode formulation allowed direct electrochemical examination of the various structures without complications from conductive additives and non-uniform mixtures. The mass loading for bulk V_2O_5 and Poly-NR electrodes was ~ 1.0 mg ± 0.2 mg. The counter electrode for all tests was lithium foil. Cyclic voltammetry was performed using a BioLogic VSP Potentiostat/Galvanostat using potential scan rates in the range 0.1 – 500 mV s^{-1}. All CVs were performed against lithium metal counter electrodes and all scans were performed in a potential window of 4.0-1.2 V. The electrolyte consisted of a 1 mol dm^{-3} solution of lithium hexafluorophosphate salts in a 1:1 (v/v) mixture of ethylene carbonate in dimethyl carbonate. The separator used in all split cell tests was a glass fiber separator (El-Cell ECC1-01-0012-A/L, 18 mm diameter, 0.65 mm thickness).

X-ray photoelectron spectroscopy was performed using a Kratos Axis 165 equipped with a monochromatic Al source (Kα = 1486.58 eV) with a spot size of 1 mm. The source

power was 150 W, the take-off angle was set normal to the sample surface, the construction and peak fittings in the narrow region spectra were performed using a Shirley type background. Adventitious carbon was used for the charge reference (C 1s) for each measurement. XRD analysis was performed using a Phillips Xpert PW3719 diffractometer using Cu Kα radiation. (Cu Kα, λ = 0.15418 nm, operation voltage 40 kV, current 40 mA).

Results and Discussion

TEM and SEM images of bulk crystalline V_2O_5 powder and poly-NRs are shown in Figure 1. The bulk V_2O_5 powder consisted of dense micron-scale particles as can be seen in Figure 1a and c. Vanadium oxide poly-NRs were prepared by thermal treatment of VONTs. As previously reported, poly-NRs consist of a granular agglomeration of nanocrystals of vanadium oxide [45] arranged in a polycrystalline nanorod architecture with internal mesoporosity. Figure 1b and d indicate that poly-NRs maintain similar nanoscale dimensions compared to their nanotube precursor, consequently poly-NRs have a far greater surface area than the bulk material. The thickness of the bulk V_2O_5 and Poly-NR material on the stainless steel substrates was ~13.68 and ~12.92 μm, respectively, as shown in tilt-corrected SEM images in Figure S1.

The core level binding energies for V $2p_{3/2}$, V $2p_{1/2}$ and O 1s acquired from V_2O_5 bulk powder and poly-NRs are shown in Figure 1e and f, respectively. The V $2p_{3/2}$ core-level is convoluted with two contributions in bulk powder, and three in poly-NRs. These contributions are assigned to V^{5+} and V^{4+} and to V^{3+} in poly-NRs. XPS allows for quantitative analysis of surface chemistry, as mentioned above, poly-NRs have a far greater surface area than the bulk particles, hence comparing the surface chemistry for both vanadium oxide samples was key for comparing their electrochemical performance. Secondly, nanoscale V_2O_3 provides a greater redox capacitance that bulk V_2O_5, allowing the distinction between capacitance and intercalation mode charge compensation to be probed

compared to the relatively smaller multivalent surface chemistry of nanoscale V_2O_5. The relative amounts of each vanadium oxidation state present on the surface of bulk V_2O_5 particles and poly-NRs are listed in Table 1. Vanadium is predominately in the V^{5+} oxidation state for bulk V_2O_5 particles, however the data quantify a near equal amount of vanadium in V^{5+} and V^{4+} oxidation states present on the surface of the poly-NRs. The V^{3+} oxidation state is also observed for poly-NRs, however it is present in the minority, comprising only ~ 21.8 %. For multivalent contributions to photoelectron emission from vanadium oxides, the average vanadium oxidation state can be determined as $13.82 - 0.68[\text{O 1s} - \text{V } 2p_{3/2}]$) [47], using the binding energies for the core levels. The average vanadium oxidation state is 5.116 for bulk V_2O_5, but 3.484 for poly-NRs in agreement with the V $2p_{3/2}$ core level spectra, indicating a highly defective surface with a higher density of O vacancies with a net multivalent surface.

	V $2p_{3/2}$		
Sample	V(V)	V(IV)	V(III)
Bulk V_2O_5	92.1 %	7.9 %	-
Poly-NRs	38.5 %	39.7 %	21.8 %

Table 1. Relative amounts of each vanadium oxidation state present on the surface of Bulk V_2O_5 and Poly-NRs from XPS.

In order to further probe the structural differences between the bulk V_2O_5 particles and the Poly-NRs, XRD patterns were obtained for each sample. The resulting XRD patterns are shown in Figure 1g and h. The XRD pattern for the bulk particles can be indexed to orthorhombic V_2O_5 (JCPDS 00-009-0387) with a *Pmmn* space grouping. The poly-NR pattern has been indexed to rhombohedral V_2O_3 (JCPDS 00-034-0187) with an *R-3c* space grouping. XPS analysis of the poly-NRs suggested that ~ 78.2 % of vanadium present in the

surface was in either a V^{5+} or V^{4+} oxidation state, however XRD analysis shows that poly-NRs are predominately V_2O_3, which would imply that vanadium is primarily in a V^{3+} oxidation state. The disparity between XPS and XRD results suggests that vanadium oxide is present in different phases on the surface and in the core of the poly-NR structure. Various vanadium oxide structures containing different bulk and surface phases have been previously reported, most notably it has been reported that heating a V_2O_5 sample for 20 hours at 500 ^oC in an H_2/He atmosphere produces V_2O_3 at the surface, a situation that is plausible by O emission from V_2O_5 that was purported to occur. [48] These conditions are quite similar to the poly-NR synthesis process.

Two additional reflections were observed in the poly-NR XRD pattern (at ~ 36.9 ^{o} and 40.2 ^{o}) which are not present in the rhombohedral V_2O_3 reference pattern. The peak at 40.2 ^{o} may be related to the vanadium oxide interplanar spacing of the nanoscale grains which comprise the poly-NR structure (*vide infra*). From XPS analysis presented in Table 1, it is clear that V^{5+}, V^{4+} and V^{3+} oxidation states are all present on the surface of the Poly-NRs. XRD confirms this and analysis shows that the core of the Poly-NRs is predominately V_2O_3, and two remaining reflections may be indexed to V_4O_7 (in Figure S2), although dominant reflections from this minority phase are not found.

To further investigate the poly-NR structure a detailed high resolution TEM examination was performed to characterize the size of the nanoparticle grains that constitute the poly-NRs morphology as well as the (001) interplanar spacing of the grain's crystalline lattice. A TEM image of one full poly-NR is shown in Figure 2a, it can be seen that the diameter of a typical poly-NR is ~ 125 nm and the length is ~ 750 nm. The granular agglomeration of nanocrystals which comprise the poly-NR structure can be seen in Figure 2b, with individual nanoparticles circled in dashed red lines. The histogram in Figure 2c, presents the variation in nanoparticle diameter over 100 individual measurements from

HRTEM images. It was found that the diameter varied from ~ 4.0 to 5.2 nm with the highest frequency of counts being observed for a diameter of ~ 4.6 nm. The layered structure of the nanoscale grains is shown in Figure 2d and the variation in the interplanar spacing is illustrated by the histogram shown in Figure 2e. The variation in the interplanar spacing over 100 individual measurements was ~ 0.06 nm, indicating that interplanar spacing of the nanoscale grains within poly-NRs is consistent throughout the material. From this statistical examination it was determined that the most frequent interplanar spacing was ~ 0.224 nm. This d-spacing corresponds to a 2θ angle of ~ 40.2 ^{o} and there is a reflection in the XRD pattern for Poly-NRs at this angle, as can be seen in Figure 1h.

It is worth noting that all electrodes used in this test were prepared by drop-casting a solution of the active material in ethanol onto the current collector and then drying. No conductive additives or binding materials were used in the preparation of the electrodes used in this study. The surface of the active material can be buried in slurry cast electrodes, which limits electrolyte access to surface redox sites. [44] Capacitive charge processes occur on the surface of the active material hence, preparing a slurry with passivating polymeric binders may impeded direct comparative assessment of each material. Likewise it can be difficult to deconvolute the electrochemical properties of the active material from the electrochemical response of the composite electrode. [49]

Cyclic voltammetry was performed on both bulk V_2O_5 and poly-NRs at a range of different scan rates. The resulting CV curves for bulk V_2O_5 are shown in Figure 3. CV scans using scan rates from 0.1 to 0.5 mV/s are shown in Figure 3a. The cathodic and anodic peaks represent lithium insertion and removal peaks respectively. Lithium insertion peaks during the initial cathodic scan at 0.1 mV/s were observed at ~3.34, 3.14, 2.32 and 1.65 V. These peaks correspond to phase transitions due to the insertion of lithium ions into the layers of vanadium oxide [18,19]. It is interesting that these discrete peaks are only observed for the

first cycle, from the second cycle onwards, two wide peaks are observed in the cathodic scans at ~3.17 and 2.00 V. This suggests that an irreversible reaction occurs during the first cycle, which is not observed in the subsequent cycles. This irreversible reaction is most likely the formation of a ω-$Li_xV_2O_5$ phase. It has been reported that for galvanostatic tests when bulk V_2O_5 is discharged below 1.9 V an irreversible phase is formed whereby not all of the intercalated lithium can be successfully removed upon subsequent charging [50,19,18]. A similar process occurred in the faster scan rate range of 1 to 5 mV/s. Discrete peaks were observed during the initial scan at a scan rate of 1 mV/s and these were replaced with wide peaks as the scan rate was increased to 5 mV/s. The distinct lithium insertion peaks observed during the initial cathodic scans at slow scan rates were not observed when the scan rate was increased to 10 and 100 mV/s as can be seen in Figure 3c and d.

Cyclic voltammograms for the poly-NR material are shown in Figure 4. From the initial voltammetric curves at 0.1 and 1 mV/s shown in Figure 4a and b, it is clear that the phase transitions (defined cathodic peaks) that were observed for bulk V_2O_5 indicating charge compensation by Li insertion and V^{5+}/V^{4+} redox couple reduction, are found to smoothen and extend over a wider potential range for poly-NRs. It has been reported that the small domain sizes offered by nanostructure materials can lead to a suppression of phase transitions due to reduced intercalation stress, from volume expansion. [49,51] Hence the smaller dimensions of the poly-NRs, detailed in Figure 2, may be the reason why the CV curves are much smoother than those observed for the bulk V_2O_5. It has also been reported that, smooth curves may be indicative of an amorphous or a cation-disordered material [52,53], or insertion into a range of nanocrystallites with random relative orientations (polycrystalline). TEM analysis and XRD analysis (Figure 1) verify that poly-NRs are indeed polycrystalline. Similar smoothness in the potential was also found in voltage profiles when poly-NRs were galvanostatically discharged and charged [45], as shown in Figure S3.

Wide lithium insertion and removal peaks were observed when poly-NRs were cycled using scan rates in the range of 0.1 – 0.5 mV/s and 1 – 5 mV/s. In both cases the lithium insertion peak was shifted to lower potentials and the lithium removal peak was shifted to higher potentials as the scan rate increased. With faster voltage scan rates, the peak current also increased as expected. At faster scan rates the CV curves smoothened further as can be seen in Figure 4c and d and the potential difference between cathodic and anodic peaks increased from ~0.4 V to 1.6 V at 10 mV/s.

The area under the CV curves represents the total stored charge during each scan, which arises from both faradaic and non-faradaic processes [31] when they occur. The specific capacity for bulk V_2O_5 and poly-NRs at various scan rates was determined from the integrated area of each curve according to

$$C = \frac{1}{mv(V_c - V_a)} \int_{V_a}^{V_c} I(V)dV,$$

where V_c and V_a are the cathodic and anodic voltage limits, respectively, and v is the scan rate as usual. The calculated specific capacities of the cathodic scan for bulk V_2O_5 and poly-NRs in a scan rate range from 0.1 to 0.5 mV/s are shown in Figure 5a. It was observed that the specific capacity is strongly dependent on the potential scan rate. As the scan rate was increased, the specific capacity was found to reduce. This effect may be due to kinetic limitations associated with the diffusion of Li^+ into thickening lithiated V_2O_5 bulk crystal surfaces ($t \sim L^2/D$). The shorter length scales in poly-NRs improve the rate of lithiation (reduction in time with invariant solid state Li^+ diffusion constant). The influence of surface defect chemistry and overall surface area on redox capacitance storage versus intercalation at slow scan rates is ill-defined in many materials (with porosity, conductivity and accessibility of electrolyte also important) and the way charge is stored is also potential-dependent. From Figure 5a it is clear that the specific capacity values obtained for poly-NRs were substantially

higher than the values obtained for bulk V_2O_5. There is a significant difference in the particle size of the two materials, as shown in Figure 1 and also the crystalline phase of the poly-NRs is that of V_2O_3, although the intercalation rate for nanoscale crystallite is not found to be markedly different to nanoscale V_2O_5; the surface chemistry and size dominantly dictate the comparative responses. For the same scan rate the total stored charge is higher for the smaller poly-NRs at similar mass loading. The nanoscale dimensions of the poly-NRs offer a larger surface area and shorter Li^+ diffusion lengths compared to the micron scale bulk particles.

The total stored charge can be separated into three components: (i) the faradaic contribution from the Li^+ transfer process, (ii) the faradaic contribution from the charge transfer process with surface atoms, referred to as redox pseudocapacitance involving the reduction of the metal (in this case V^{5+} and V^{4+} species reduction), but with no electrochemically driven phase transition in the crystal, and (iii) the non-faradaic contribution at the double layer [29]. These effects in nanoscale materials, particularly layered, multivalent vanadium oxides, are important in correctly analysing cycling and specific capacities under potentiodynamic conditions when used as battery positive electrodes [54-56]. Capacitive effects due to pseudocapacitance and double layer charging can be characterized by analysing CV curves at various scan rates according to [36]

$$i(V,t) = av^b$$

where the measured current *i* obeys a power law relationship with the scan rate *v*. Both *a* and *b* are adjustable parameters, *b*-exponent values are determined from the slope of the plot of log (*i*) vs log (*v*). There are two well defined conditions for *b*: $b = 0.5$ and $b = 1.0$. When $b = 0.5$, the current response is said to be limited by semi-infinite diffusion, which is indicative of a faradaic process that may include intercalation, alloying etc. When $b = 1.0$, the current response is representative of a capacitive response [40]. A plot of log (*i*) vs log (*v*) for bulk

V_2O_5 and poly-NRs at 1.65 V is shown in Figure 5b, this potential corresponds to the lowest potential cathodic peak for bulk V_2O_5, as can be seen in Figure 3a. The corresponding *b*-values for bulk V_2O_5 and poly-NRs at 1.65 V were determined to be ~0.93 and ~0.56, respectively. This suggests that at 1.65 V the current response for bulk V_2O_5 is primarily capacitive in nature whereas the current for poly-NRs at the same potential is due to intercalation reactions. As detailed earlier, the specific capacity of poly-NRs under galvanostatic discharge is ~ 280 mAh g^{-1}. The total integrated charge values shown in Figure 5a ranges from 475 mAh g^{-1} at 0.1 mV/s to 250 mAh g^{-1} at 0.5 mV/s.

The *b*-values for bulk V_2O_5 and poly-NRs from 3.1 – 1.2 V are shown in Figure 5c and (d) respectively and are overlaid on the first cathodic scan for each sample at a scan rate of 0.1 mV/s. We observed two discrete lithium insertion peaks in the cathodic scan for bulk V_2O_5 at ~2.32 and 1.65 V, as shown in Figure 5c, which correspond to δ-$Li_1V_2O_5$ and ω-$Li_3V_2O_5$ by comparison to the galvanostatic discharge profiles/phase transitions [57,58,50,59]. The *b*-values in the potential range of 2.64 – 2.12 V are ~0.4, indicating that the peak observed at 2.32 V arises predominantly from intercalation mode effects. The *b*-values in the potential range of 1.86 – 1.33 V are ~0.8, indicating that the peak observed at 1.65 V arises predominantly from capacitive effects, this potential range also corresponds to the phase transition from δ-$Li_xV_2O_5$ to γ-$Li_xV_2O_5$ [60]. These *b*-exponents indicate that the measured current for a cathodic scan for bulk V_2O_5 contains two distinct regions: (i) from 3.1 – 2.0 V, the current response is primarily due to intercalation and (ii) from 2.0 – 1.2 V, the current response is primarily due to capacitive mode charge storage. A different response was observed for poly-NRs as shown in Figure 5d. The average *b*-value from 3.1 – 1.2 V was ~ 0.60 indicating that the measured current was primarily due to intercalation reactions. The highest *b*-value obtained was ~0.69, which occurred at 2.24 V, and suggests that, during the cathodic scan, the current arises from diffusion controlled Li^+ insertion reactions mixed with

contributions from capacitive effects. However the *b*-values indicate that the majority fraction of the total stored charge is due to intercalation mode processes. As mentioned above there are two well defined conditions for *b*. However *b*-values other than these have previously been reported. [40,31,61,17,49] It is quite common for *b*-values to be limited to a selected range of the potential window, as opposed to the full voltage range, most likely because *b*-values outside of this range may be either >0.5 or >1.0. Also, the *b*-values are calculated for a few points along this decreased potential window. Herein, we present *b*-values which have been calculated at every potential along cathodic scan (with similar voltage resolution as the scan rate) and consequently the *b*-values are presented as a smooth line, and in the case of the bulk V_2O_5 particles *b*-values which are below 0.5 are presented.

From analysis of CV curves obtained at various scan rates it is possible to determine quantitatively the diffusion-based intercalation and capacitive contributions to the current response. The current response *i*, at a fixed potential *V* can be described as the combination of capacitive effects (k_1v) and diffusion controlled insertion ($k_2v^{1/2}$) according to [62,35]:

$$i(V,t) = k_1 v + k_2 v^{1/2}$$

where *v* is the scan rate. By determining k_1 and k_2 it is possible to distinguish between the currents arising from Li^+ insertion and those occurring from capacitive processes. The voltage profiles for the intercalation (blue area) and capacitive (red area) currents were compared with the total measured current (grey area) for bulk V_2O_5 and poly-NRs for scan rates in the range 0.1 - 100 mV/s, as shown in Figure 6. Note, that electrode polarization effects at higher scan rates that cause a sloping of the overall voltammogram are not accounted for in the analysis. Anodic capacitive processes do not occur in parallel with cathodic intercalation processes in the actual electrode. For bulk V_2O_5, at a scan rate of 0.1 mV/s, there is a wide peak in the capacitive curve at ~ 1.75 V, this is in agreement with the *b*-

values calculated for bulk V_2O_5, shown in Figure 5c. At 1.75 V the calculated *b*-value was ~ 0.90 which indicates that the measured current at that potential was primarily from capacitive effects, even at slow potential scan rates. This broad peak may also be indicative of a charge-transfer process similar to intercalation pseudocapacitance [40,63]. Importantly, while slow scan rates for any size material are often ascribed to intercalation reactions and processes similar to those found under galvanostatic conditions, the *b*-exponent analysis confirms that for large crystals of active material, the electrochemical response should not be pre-emptively ascribed to diffusion-limited insertion, intercalation, or alloying processes by default at all voltages under voltammetric polarization.

A larger contribution from intercalation effects can be seen in the CV curves for poly-NRs compared to bulk V_2O_5 in similar potential ranges at slow scan rates (Figure S4). As previously mentioned, poly-NRs have a significantly larger surface area and a richer multivalent surface chemistry than bulk V_2O_5 particles and their nanoscale dimensions allow shorter Li^+ diffusion lengths. Hence, there was a larger contribution from intercalation to the measured current for poly-NRs. This observation is in close agreement with the *b*-values calculated for poly-NRs. The average *b*-value for poly-NRs was ~0.60, indicating that intercalation processes were dominating the contribution to the measured current. At transition metal oxide surfaces including vanadium oxide, pseudocapacitive contributions from redox processes with Li^+, particularly with O-vacancy defective high surface area poly-NRs [37], can significantly contribute to the overall electrochemical energy storage mechanism at higher potentials, compared to larger bulk crystals, whose capacitive charge at similar scan rates is observed at lower potentials. At the higher scan rates (1-100 mV s^{-1}), we find a size and surface chemistry influence on the energy storage mechanism over the entire potential range. From Figure 6, a dominance of intercalation is found at higher scan rates for the poly-NRs, confirming that at all potentials, reduced size accommodates intercalation even

at faster potential scan rates, with less capacitive contributions at any potential or slower scan rate, for nanoscale vanadium oxide.

The specific capacity and the relative contributions associated with lithium insertion and capacitive processes for bulk V_2O_5 and poly-NRs for the cathodic section of each scan were calculated from the data in Figure 3 and 4. The intercalation and capacitive contributions towards the total cathodic specific capacity for bulk V_2O_5 and poly-NRs are shown in Figure 7. The data presented in Figure 7 was acquired from four separate CV scans for bulk V_2O_5 and poly-NRs, in four separate scan rate ranges. Thus, there is an increase in the specific capacity for both materials at 1, 10 and 100 mV/s, which also provides an opportunity to observe the capacity fade under potentiodynamic condition in each scan rate range, while providing the relative capacitive to intercalation-mode contributions to this capacity. For bulk V_2O_5, the % specific capacity due to intercalation processes increased as the scan rate increased, from 75.3 % at 0.1 mV/s to 78.5 % at 100 mV/s, as shown in Figure 7a. The contribution due to intercalation processes increased further for poly-NRs, from 82.7 % at 0.1 mV/s to 93.3 % at 100 mV/s (Figure 7b). The increased contribution from intercalation processes at faster scan rates for poly-NRs compared to bulk V_2O_5 is most likely due to the smaller poly-NR particle size in spite of a richer surface chemistry that often facilitates surface redox capacitance at the surface. The larger bulk particles have longer Li^+ diffusion lengths within the crystal to unreacted V_2O_5 lattice sites during discharge compared to poly-NRs, consequently at faster scan rates the diffusion and subsequent intercalation processes occur to the same extent over different time scales ($\sim t^{1/2}$ for intercalation, $\sim t$ for capacitive contributions), which may account for the decreased intercalation contribution. A recent study [64] confirmed that nanoscale V_2O_5 with dimensions <10 nm on carbon backbone structures began to show capacitive-like effects. Here, we unequivocally

determined the rate dependence for nanoscale V_2O_5 with defined defect chemistry, compared to bulk materials, and also as a function of the applied potential.

The contribution due to cation intercalation and phase conversion processes increased with increased scan rate, consequently the % of specific capacity due to capacitive effects (redox and any intercalation pseudocapacitance without a phase change) reduced. For bulk V_2O_5 the capacitive contribution significantly decreased from ~89.0 to 33.0 mAh g^{-1} for scan rates from 0.1 to 100 mV/s and for poly-NRs the capacitive contribution decreased even further from ~80.7 to 5.7 mAh g^{-1}. This suggests that for both bulk micron scale V_2O_5 particles and nanoscale vanadium oxide poly-NRs capacitive charge storage becomes less significant at fast scan rates (100 mV/s). When cycled at slower scan rates (0.1 – 0.5 mV/s), the specific capacity contribution due to capacitive processes (in mAh g^{-1}) remained almost unchanged with increased scan rate, as shown in Figure 7a and b. For bulk V_2O_5 the capacitive contribution decreased from ~89.0 to 70.4 mAh g^{-1} for scan rates from 0.1 to 0.5 mV/s and for poly-NRs the capacitive contribution decreased from ~80.7 to 78.4 mAh g^{-1}. This suggests that at slow scan rates, capacitive contributions are not significantly affected by increased cycling at successively faster scan rates. The capacitive processes may not be as destructive to both bulk V_2O_5 and poly-NRs as the intercalation process can be.

It is clear from Figure 7 that over a wide range of scan rates, contributions to the measured current from intercalation processes are dominant for both bulk V_2O_5 and poly-NRs. This implies that engineering micron-scale bulk V_2O_5 particles with primarily one valence to form nanoscale multivalent vanadium oxide poly-NRs does not result in capacitive processes dominating over intercalation processes when cycled electrochemically. As discussed earlier, poly-NRs are comprised of nanoscale grains of vanadium oxide. The capacitive and intercalative contributions towards the total stored charge for poly-NR electrodes presented in Figure 7(b) suggests that at faster potential scan rates there is a

preference for intercalation charge storage which is most likely being facilitated by the reduced diffusion path lengths of the poly-NRs. Consequently, for poly-NR samples the capacitive contribution decreases with increasing scan rates.

We note that the nanoscale form of the material is the V_2O_3 phase, which does not possess the dominant layered, cation-insertion regions of V_2O_5, yet the reduced dimension in certain voltage ranges and scan rates promote intercalation over capacitance storage even for the highly multivalent surface. This is an important finding as it suggests that making a material smaller and altering its phase does not automatically result in a shift towards pseudocapacitive behaviour even under faster voltage sweeps, as has been reported for TiO_2 [31] and MoO_3 [40]. It was previously suggested by Simon et al. [15] that preparing nanoscale forms of battery materials does not necessarily transform them into oxide supercapacitors because their faradaic redox peaks and galvanostatic profiles remain battery-like. This suggestion is in good agreement with our results whereby preparing a nanoscale vanadium oxide structure did not result in a domination of capacitive charge storage.

A schematic representation of the proposed charge storage mechanisms during cyclic voltammetry for bulk V_2O_5 particles and poly-NRs is shown in Figure 8. At fast scan rates (~100 mV/s), a lower quantity of Li^+ ions are inserted into the larger bulk V_2O_5 particles than the poly-NRs, due to the increased surface area and shorter Li^+ diffusion path lengths of the nanorods. Consequently, more specific charge is stored due to diffusion processes for poly-NRs than for the bulk particles. It may be expected that there would be a significant increase in surface charge storage with increased surface area for poly-NRs, however their nanoscale dimensions also provide shorter diffusion lengths with more regions in direct contact with the electrolyte and hence, the diffusion process dominates.

By comparing reveal that the response of small, high surface area, multivalent oxides to lithium insertion at different rates and voltages include both intercalation and capacitive contributions to the total stored charge. While the approach is applicable to any material in principle, proper evaluation of new and existing materials and their charge storage mechanisms is important in distinguishing the true performance metrics of materials and the nature of the Fardaic and non-Faradaic capacitance processes in electrochemical energy storage materials.

Conclusions

From cyclic voltammetry analysis of bulk V_2O_5 crystals and vanadium oxide polycrystalline nanorods at a wide range of potential scan rates, we determined that the specific capacity (total stored charge) for poly-NRs was significantly higher than for bulk V_2O_5.The quantitative contribution due to intercalation processes and capacitive contributions to the total stored charge was determined for each material by analysis of the measured current versus the rate of change of discharge and charging potentials. The measured current for the micron-scale bulk particles exhibited a larger contribution from capacitive effects than the nano-scale vanadium oxide poly-NRs at the same scan rates even though the nanorods were found to exhibit a richer surface chemistry with multiple V^{5+}/V^{4+} and V^{4+}/V^{3+} redox couples. This is in close agreement with *b*-values determined from the power law dependence of current on scan rate and shows that by using a nano-scale vanadium oxide structure and increasing the surface area, does not significantly increase pseudocapacitive behaviour. This is most likely due to the shorter Li^+ diffusion path lengths available to the nanoscale poly-NRs and a preference for intercalation compared to surface redox pseudocapacitance with multivalent surface species.

Four key findings from this study are as follows: (i) Charge storage for V_2O_5 structures is not exclusively due to intercalation processes, capacitive charge storage also occurs, (ii) Capacitive effects are more significant at slower scan rates for vanadium oxide materials of bulk and nanoscale size irrespective of phase, (iii) The measured current for bulk V_2O_5 materials and also V_2O_3 nanoscale poly-NRs is predominately due to diffusion processes at all potentials. Considerable capacitive contribution to multivalent nanoscale materials is found above 3 V for poly-NRs at slow scan rates where the multivalent surface chemistry dominates over short solid state diffusion distances for cations, (iv) Making a vanadium oxide structures smaller, and increasing the surface area does not automatically significantly increase its (redox) pseudocapacitive behaviour at any scan rate, as determined from capacitive contributions towards the measured current.

Acknowledgements

This publication has emanated from research conducted with the financial support of the Charles Parsons Initiative and Science Foundation Ireland (SFI) under Grant No. 06/CP/E007. Part of this work was conducted under the framework of the INSPIRE programme, funded by the Irish Government's Programme for Research in Third Level Institutions, Cycle 4, National Development Plan 2007-2013. We acknowledge support from Science Foundation Ireland under a Technology Innovation and Development Award no. 13/TIDA/E2761. This research has received funding from the Seventh Framework Programme FP7/2007-2013 (Project STABLE) under grant agreement no. 314508. This publication has also emanated from research supported in part by a research grant from SFI under Grant 14/IA/2581.

References

1. Croguennec L, Palacin MR (2015) Recent Achievements on Inorganic Electrode Materials for Lithium-Ion Batteries. Journal of the American Chemical Society 137:3140-3156.
2. Etacheri V, Marom R, Elazari R, Salitra G, Aurbach D (2011) Challenges in the development of advanced Li-ion batteries: a review. Energy & Environmental Science 4:3243-3262.
3. Scrosati B, Garche J (2010) Lithium batteries: Status, prospects and future. Journal of Power Sources 195:2419-2430.
4. McSweeney W, Geaney H, O'Dwyer C (2014) Metal assisted chemical etching of silicon and the behaviour of nanoscale silicon materials as Li-ion battery anodes. Nano Research 8:1395.
5. Johnson CS, Li N, Lefief C, Vaughey JT, Thackeray MM (2008) Synthesis, Characterization and Electrochemistry of Lithium Battery Electrodes: $xLi_2MnO_3\cdot(1-x)LiMn_{0.333}Ni_{0.333}Co_{0.333}O_2$ ($0 \leq x \leq 0.7$). Chemistry of Materials 20:6095-6106.
6. Hu L, Wu H, La Mantia F, Yang Y, Cui Y (2010) Thin, flexible secondary Li-ion paper batteries. ACS Nano 4:5843-5848.
7. Gu M, Belharouak I, Zheng J, Wu H, Xiao J, Genc A, Amine K, Thevuthasan S, Baer DR, Zhang J-G, Browning ND, Liu J, Wang C (2013) Formation of the Spinel Phase in the Layered Composite Cathode Used in Li-Ion Batteries. ACS Nano 7:760-767.
8. Bruce PG, Scrosati B, Tarascon J-M (2008) Nanomaterials for Rechargeable Lithium Batteries. Angewandte Chemie International Edition 47:2930-2946.
9. Arico AS, Bruce P, Scrosati B, Tarascon J-M, van Schalkwijk W (2005) Nanostructured materials for advanced energy conversion and storage devices. Nat Mater 4:366-377.
10. Osiak M, Geaney H, Armstrong E, O'Dwyer C (2014) Structuring materials for lithium-ion batteries: advancements in nanomaterial structure, composition, and defined assembly on cell performance. Journal of Materials Chemistry A 2:9433-9460.
11. Gogotsi Y (2014) What Nano Can Do for Energy Storage. ACS Nano 8:5369-5371.
12. Liu N, Hu L, McDowell MT, Jackson A, Cui Y (2011) Prelithiated Silicon Nanowires as an Anode for Lithium Ion Batteries. ACS Nano 5:6487-6493.
13. Reddy ALM, Srivastava A, Gowda SR, Gullapalli H, Dubey M, Ajayan PM (2010) Synthesis Of Nitrogen-Doped Graphene Films For Lithium Battery Application. ACS Nano 4:6337-6342.
14. Wang D, Choi D, Li J, Yang Z, Nie Z, Kou R, Hu D, Wang C, Saraf LV, Zhang J, Aksay IA, Liu J (2009) Self-Assembled TiO_2–Graphene Hybrid Nanostructures for Enhanced Li-Ion Insertion. ACS Nano 3:907-914.
15. Simon P, Gogotsi Y, Dunn B (2014) Where Do Batteries End and Supercapacitors Begin? Science 343:1210-1211.
16. Augustyn V, Simon P, Dunn B (2014) Pseudocapacitive oxide materials for high-rate electrochemical energy storage. Energy & Environmental Science 7:1597-1614.
17. Augustyn V, Come J, Lowe MA, Kim JW, Taberna P-L, Tolbert SH, Abruña HD, Simon P, Dunn B (2013) High-rate electrochemical energy storage through Li^+ intercalation pseudocapacitance. Nat Mater 12:518-522.
18. McNulty D, Buckley DN, O'Dwyer C (2014) Synthesis and electrochemical properties of vanadium oxide materials and structures as Li-ion battery positive electrodes. Journal of Power Sources 267:831-873.
19. Whittingham MS (1976) The role of ternary phases in cathode reactions. Journal of The Electrochemical Society 123:315-320.
20. Whittingham MS (2004) Lithium Batteries and Cathode Materials. Chemical Reviews 104:4271-4302.

21. Periyapperuma K, Tran TT, Trussler S, Ioboni D, Obrovac M (2014) Conflat Two and Three Electrode Electrochemical Cells. Journal of The Electrochemical Society 161:A2182-A2187.
22. Qin M, Liang Q, Pan A, Liang S, Zhang Q, Tang Y, Tan X (2014) Template-free synthesis of vanadium oxides nanobelt arrays as high-rate cathode materials for lithium ion batteries. Journal of Power Sources 268:700-705.
23. Shao J, Li X, Wan Z, Zhang L, Ding Y, Zhang L, Qu Q, Zheng H (2013) Low-Cost Synthesis of Hierarchical V2O5 Microspheres as High-Performance Cathode for Lithium-Ion Batteries. ACS Applied Materials & Interfaces 5:7671-7675.
24. Chen X, Zhu H, Chen Y-C, Shang Y, Cao A, Hu L, Rubloff GW (2012) MWCNT/V2O5 Core/Shell Sponge for High Areal Capacity and Power Density Li-Ion Cathodes. ACS Nano 6:7948-7955.
25. O'Dwyer C, Navas D, Lavayen V, Benavente E, Santa Ana MA, Gonzalez G, Newcomb SB, Torres CMS (2006) Nano-urchin: The formation and structure of high-density spherical clusters of vanadium oxide nanotubes. Chemistry of Materials 18:3016-3022.
26. O'Dwyer C, Lavayen V, Newcomb SB, Ana MAS, Benavente E, Gonzalez G, Torres CMS (2007) Vanadate conformation variations in vanadium pentoxide nanostructures. Journal of the Electrochemical Society 154:K29-K35.
27. O'Dwyer C, Lavayen V, Tanner DA, Newcomb SB, Benavente E, Gonzalez G, Torres CMS (2009) Reduced Surfactant Uptake in Three Dimensional Assemblies of VO(x) Nanotubes Improves Reversible Li(+) Intercalation and Charge Capacity. Adv Funct Mater 19:1736-1745.
28. Carrasco J (2014) Role of van der Waals Forces in Thermodynamics and Kinetics of Layered Transition Metal Oxide Electrodes: Alkali and Alkaline-Earth Ion Insertion into V2O5. The Journal of Physical Chemistry C 118:19599-19607.
29. Conway BE, Birss V, Wojtowicz J (1997) The role and utilization of pseudocapacitance for energy storage by supercapacitors. Journal of Power Sources 66:1-14.
30. Gwon H, Hong J, Kim H, Seo D-H, Jeon S, Kang K (2014) Recent progress on flexible lithium rechargeable batteries. Energy & Environmental Science 7:538-551.
31. Wang J, Polleux J, Lim J, Dunn B (2007) Pseudocapacitive contributions to electrochemical energy storage in TiO2 (anatase) nanoparticles. The Journal of Physical Chemistry C 111:14925-14931.
32. Marschilok AC, Davis SM, Leising RA (2001) Silver vanadium oxides and related battery applications. Coordination Chemistry Reviews 219:283-310.
33. Miller JR, Simon P (2008) Electrochemical capacitors for energy management. Science Magazine 321:651-652.
34. Long JW, Bélanger D, Brousse T, Sugimoto W, Sassin MB, Crosnier O (2011) Asymmetric electrochemical capacitors—Stretching the limits of aqueous electrolytes. MRS Bulletin 36:513-522.
35. Huang C, Grant PS (2013) One-step spray processing of high power all-solid-state supercapacitors. Scientific reports 3.
36. Lindström H, Södergren S, Solbrand A, Rensmo H, Hjelm J, Hagfeldt A, Lindquist S-E (1997) Li+ Ion Insertion in TiO2 (Anatase). 2. Voltammetry on Nanoporous Films. The Journal of Physical Chemistry B 101:7717-7722.
37. Rolison DR, Nazar LF (2011) Electrochemical energy storage to power the 21st century. MRS Bulletin 36:486-493.
38. Beasley CA, Sassin MB, Long JW (2015) Extending Electrochemical Quartz Crystal Microbalance Techniques to Macroscale Electrodes: Insights on Pseudocapacitance Mechanisms in MnOx-Coated Carbon Nanofoams. Journal of The Electrochemical Society 162:A5060-A5064.

39. Wang X, Li X, Sun X, Li F, Liu Q, Wang Q, He D (2011) Nanostructured NiO electrode for high rate Li-ion batteries. Journal of Materials Chemistry 21:3571-3573.
40. Brezesinski T, Wang J, Tolbert SH, Dunn B (2010) Ordered mesoporous [alpha]-MoO3 with iso-oriented nanocrystalline walls for thin-film pseudocapacitors. Nature materials 9:146-151.
41. Armstrong E, McNulty D, Geaney H, O'Dwyer C (2015) Electrodeposited Structurally Stable V2O5 Inverse Opal Networks as High Performance Thin Film Lithium Batteries. ACS Appl Mater Interfaces 7:27006-27015.
42. Ghosh A, Ra EJ, Jin M, Jeong HK, Kim TH, Biswas C, Lee YH (2011) High Pseudocapacitance from Ultrathin V2O5 Films Electrodeposited on Self-Standing Carbon-Nanofiber Paper. Adv Funct Mater 21:2541-2547.
43. Li HB, Yu MH, Wang FX, Liu P, Liang Y, Xiao J, Wang CX, Tong YX, Yang GW (2013) Amorphous nickel hydroxide nanospheres with ultrahigh capacitance and energy density as electrochemical pseudocapacitor materials. Nat Commun 4:1894.
44. Dong W, Rolison DR, Dunna B (2000) Electrochemical properties of high surface area vanadium oxide aerogels. Electrochemical and Solid-State Letters 3:457-459.
45. McNulty D, Buckley D, O'Dwyer C (2014) Polycrystalline Vanadium Oxide Nanorods: Growth, Structure and Improved Electrochemical Response as a Li-Ion Battery Cathode Material. Journal of The Electrochemical Society 161:A1321-A1329.
46. McNulty D, Buckley DN, O'Dwyer C (2013) Structural and Electrochemical Characterization of Thermally Treated Vanadium Oxide Nanotubes for Li-Ion Batteries. ECS Transactions 50:165-174.
47. Gannon G, O'Dwyer C, Larsson JA, Thompson D (2011) Interdigitating Organic Bilayers Direct the Short Interlayer Spacing in Hybrid Organic–Inorganic Layered Vanadium Oxide Nanostructures. The Journal of Physical Chemistry B 115:14518-14525.
48. Mendialdua J, Casanova R, Barbaux Y (1995) XPS studies of V2O5, V6O13, VO2 and V2O3. Journal of Electron Spectroscopy and Related Phenomena 71:249-261.
49. Rauda IE, Augustyn V, Dunn B, Tolbert SH (2013) Enhancing pseudocapacitive charge storage in polymer templated mesoporous materials. Accounts of chemical research 46:1113-1124.
50. Delmas C, Brèthes S, Ménétrier M (1991) ω-LixV2O5 — a new electrode material for rechargeable lithium batteries. Journal of Power Sources 34:113-118.
51. Brezesinski K, Haetge J, Wang J, Mascotto S, Reitz C, Rein A, Tolbert SH, Perlich J, Dunn B, Brezesinski T (2011) Ordered Mesoporous α-Fe2O3 (Hematite) Thin-Film Electrodes for Application in High Rate Rechargeable Lithium Batteries. Small 7:407-414.
52. Gogotsi Y, Simon P (2011) True Performance Metrics in Electrochemical Energy Storage. Science 334:917-918.
53. Lee J, Urban A, Li X, Su D, Hautier G, Ceder G (2014) Unlocking the Potential of Cation-Disordered Oxides for Rechargeable Lithium Batteries. Science 343:519-522.
54. Cao AM, Hu JS, Liang HP, Wan LJ (2005) Self-Assembled Vanadium Pentoxide (V2O5) Hollow Microspheres from Nanorods and Their Application in Lithium-Ion Batteries. Angewandte Chemie International Edition 44:4391-4395.
55. Wang Y, Cao G (2008) Developments in Nanostructured Cathode Materials for High-Performance Lithium-Ion Batteries. Advanced Materials 20:2251-2269.
56. Wang Y, Takahashi K, Lee KH, Cao G (2006) Nanostructured Vanadium Oxide Electrodes for Enhanced Lithium-Ion Intercalation. Adv Funct Mater 16:1133-1144.
57. Delmas C, Cognac-Auradou H, Cocciantelli JM, Ménétrier M, Doumerc JP (1994) The LixV2O5 system: An overview of the structure modifications induced by the lithium intercalation. Solid State Ionics 69:257-264.

58. Cava RJ, Santoro A, Murphy DW, Zahurak SM, Fleming RM, Marsh P, Roth RS (1986) The structure of the lithium-inserted metal oxide δLiV2O5. Journal of Solid State Chemistry 65:63-71.
59. Leger C, Bach S, Soudan P, Pereira-Ramos J-P (2005) Structural and Electrochemical Properties of ω Li x V 2 O 5 (0.4⩽ x⩽ 3) as Rechargeable Cathodic Material for Lithium Batteries. Journal of The Electrochemical Society 152:A236-A241.
60. Cocciantelli JM, Doumerc JP, Pouchard M, Broussely M, Labat J (1991) Crystal chemistry of electrochemically inserted LixV2O5. Journal of Power Sources 34:103-111.
61. Brezesinski T, Wang J, Polleux J, Dunn B, Tolbert SH (2009) Templated nanocrystal-based porous TiO2 films for next-generation electrochemical capacitors. Journal of the American Chemical Society 131:1802-1809.
62. Li G, Zhang C, Peng H, Chen K (2009) One-Dimensional V2O5@ Polyaniline Core/Shell Nanobelts Synthesized by an In situ Polymerization Method. Macromolecular rapid communications 30:1841-1845.
63. Zukalová M, Kalbáč M, Kavan L, Exnar I, Graetzel M (2005) Pseudocapacitive Lithium Storage in TiO2(B). Chemistry of Materials 17:1248-1255.
64. Sathiya M, Prakash A, Ramesha K, Tarascon JM, Shukla A (2011) V2O5-anchored carbon nanotubes for enhanced electrochemical energy storage. Journal of the American Chemical Society 133:16291-16299.

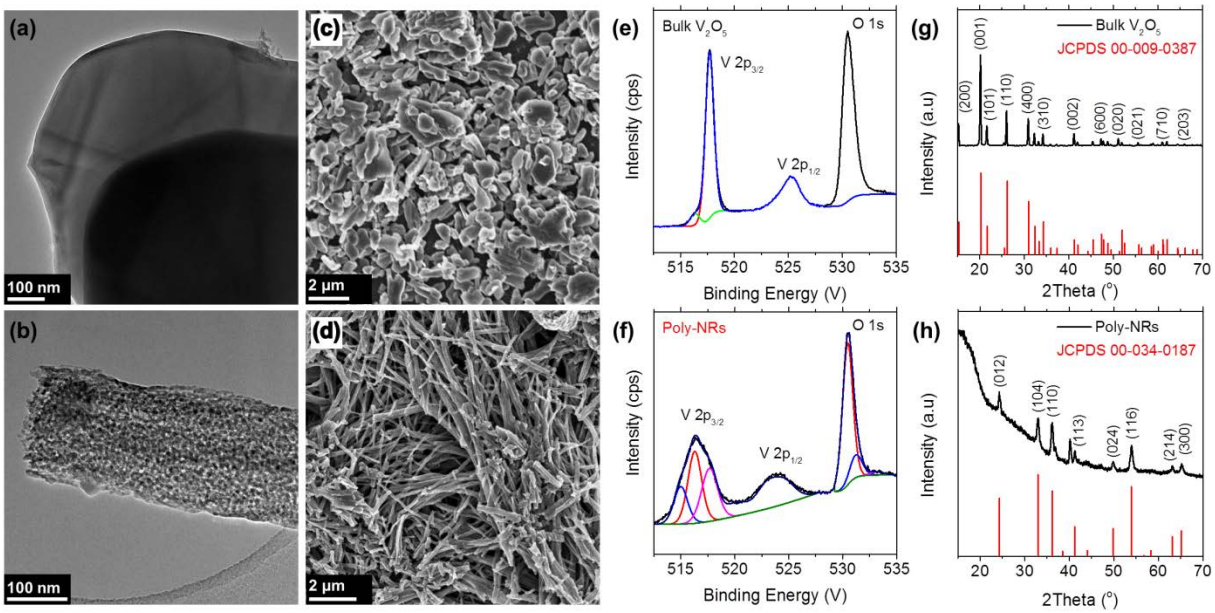

Figure 1. TEM images of (a) bulk V_2O_5 and (b) poly-NRs. SEM images of (c) bulk V_2O_5 and (d) poly-NRs. XPS V 2p and O 1s core-level emission spectra (e) of V_2O_5 bulk crystals and (f) of poly-NRs. XRD pattern of (g) bulk V_2O_5 and (h) poly-NRs.

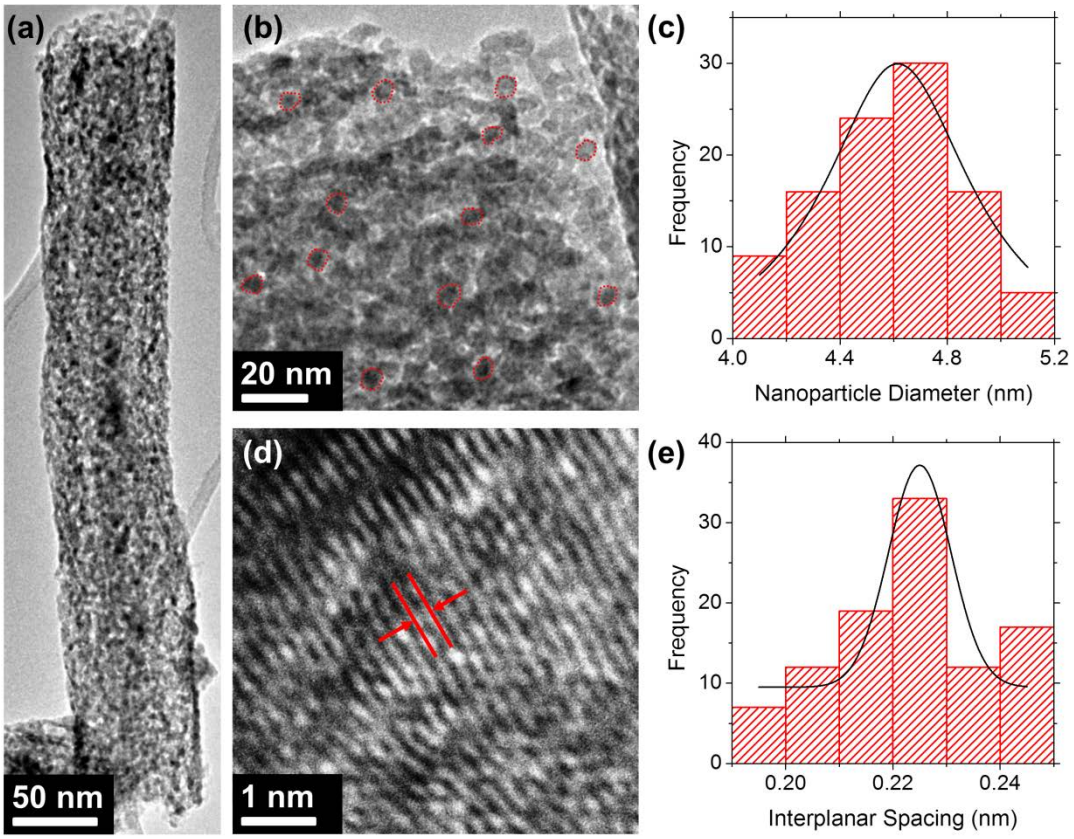

Figure 2. (a) TEM image of a typical poly-NR, (b) TEM image showing vanadium oxide nanoparticles which comprise the poly-NRs, (c) Frequency of nanoparticle diameter, (d) TEM image showing the vanadium oxide interplanar spacing present in poly-NRs (e) Frequency of vanadium oxide interplanar spacing.

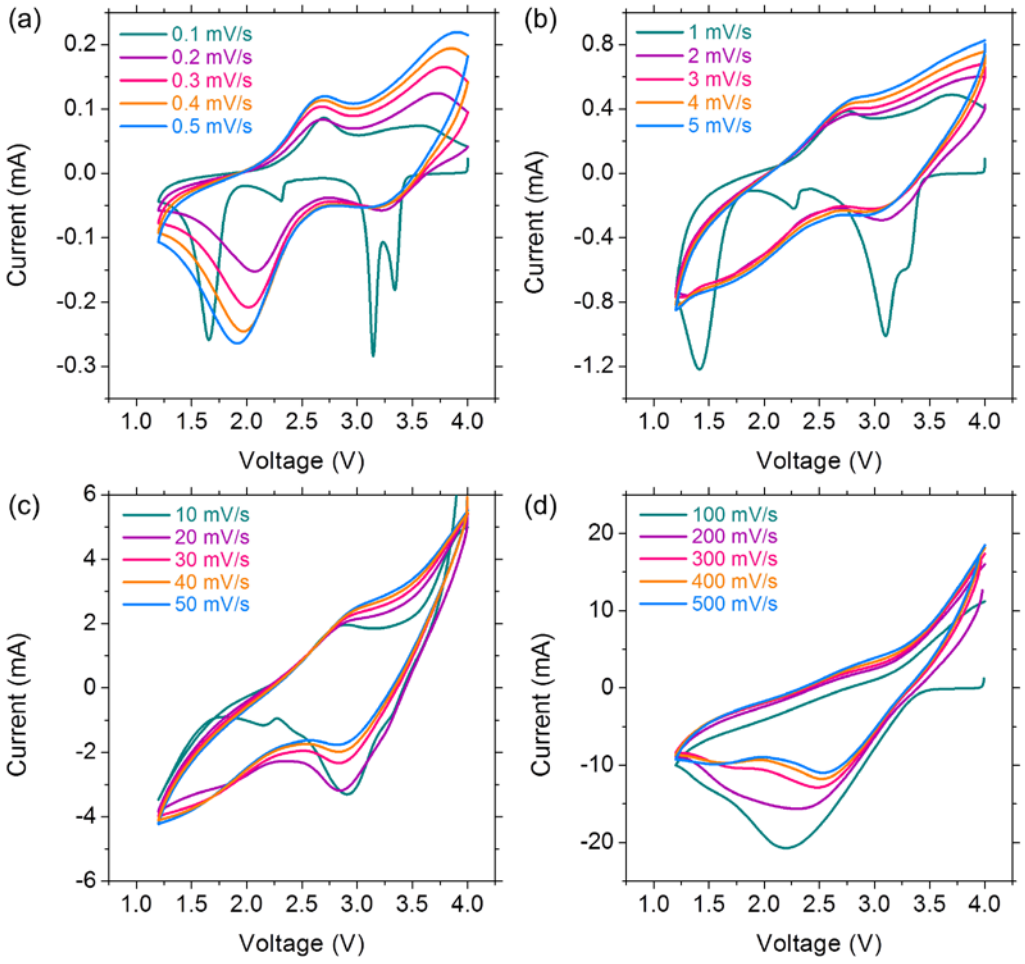

Figure 3. Cyclic voltammograms of bulk V_2O_5 at various scan rates: (a) 0.1 – 0.5 mV/s, (b) 1 – 5 mV/s, (c) 10 – 50 mV/s, (d) 100 – 500 mV/s.

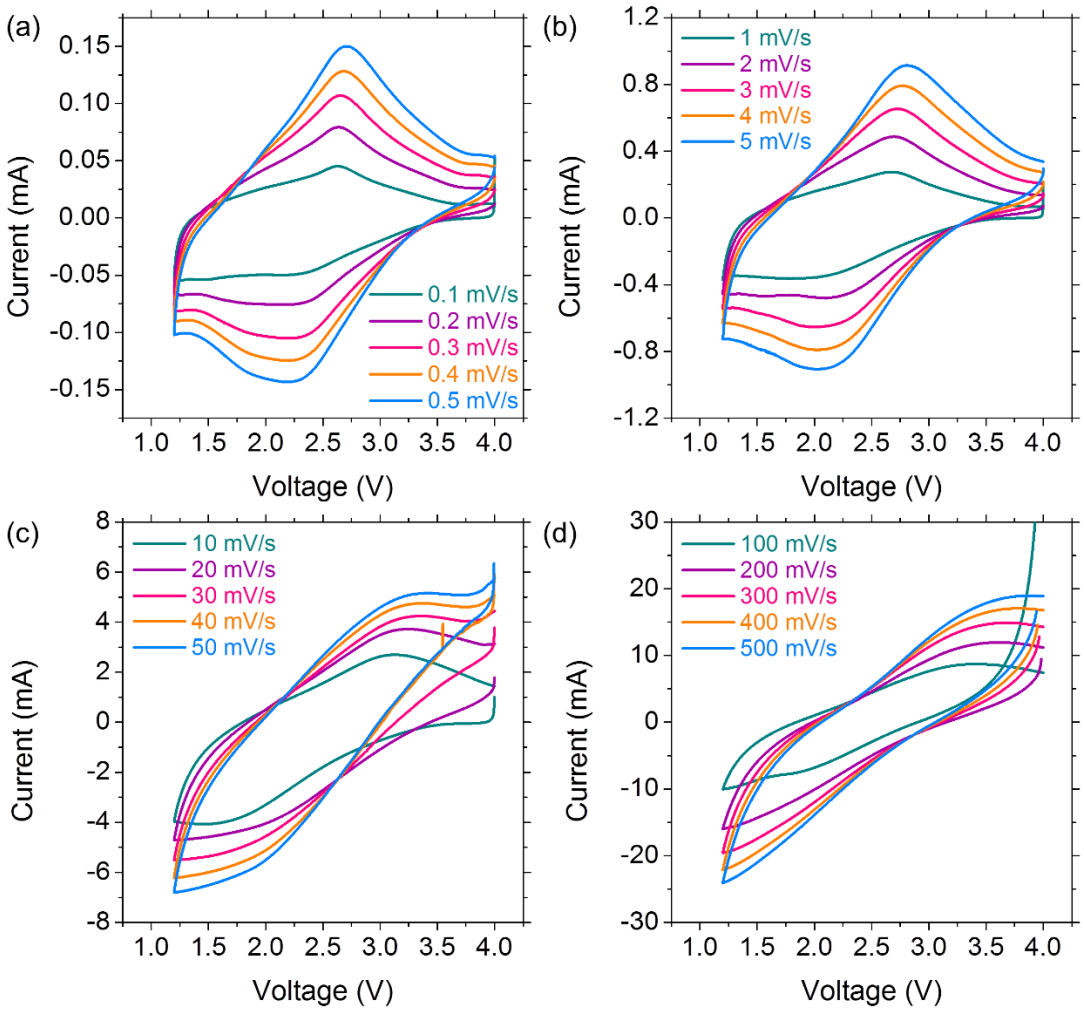

Figure 4. Cyclic voltammograms of poly-NRs at various scan rates: (a) 0.1 – 0.5 mV/s, (b) 1 – 5 mV/s, (c) 10 – 50 mV/s, (d) 100 – 500 mV/s.

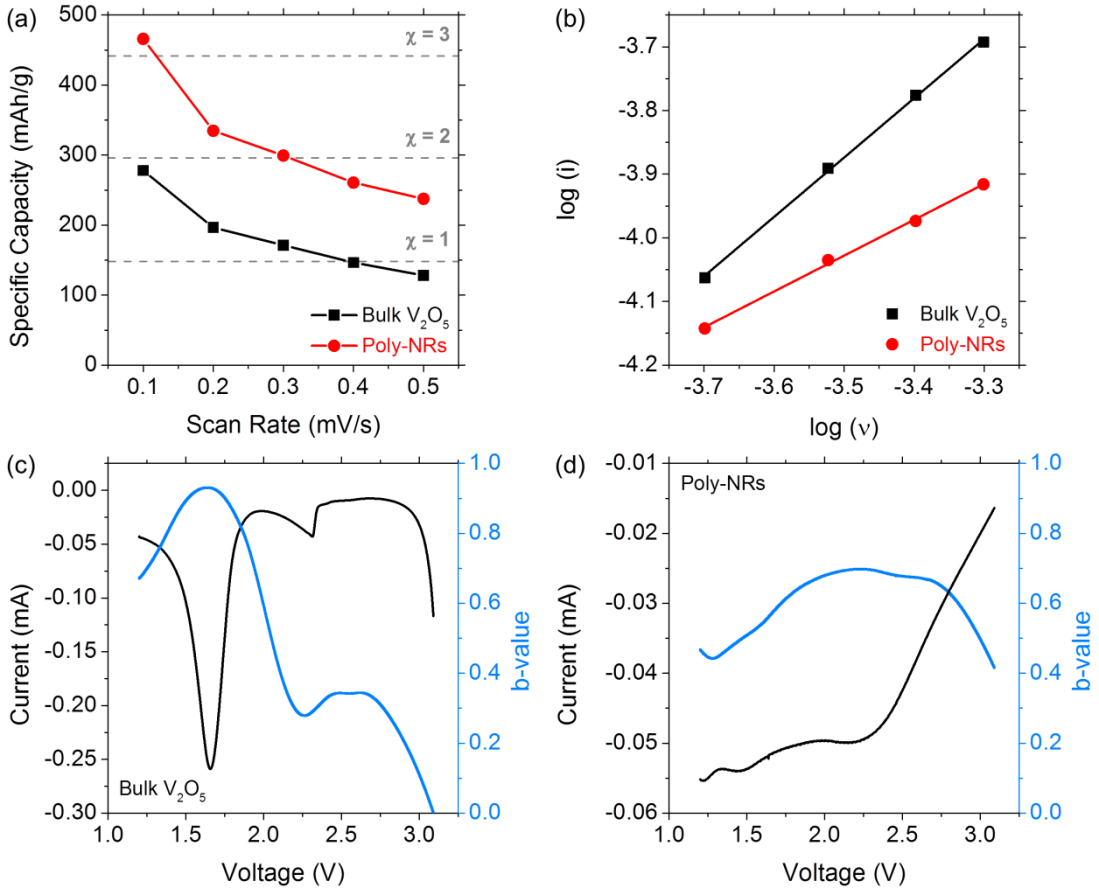

Figure 5. (a) Specific capacity as a function of scan rate for bulk V_2O_5 and poly-NRs. (theoretical capacities for $Li_XV_2O_5$, where x = 1,2,3 are shown with dashed lines) (b) log (*i*) as a function of log (*v*) for bulk V_2O_5 and poly-NRs at 1.65 V in the cathodic scan. Calculated *b*-values for (c) bulk V_2O_5 and (d) poly-NRs, overlaid on the first cathodic scan for each sample at a scan rate of 0.1 mV/s.

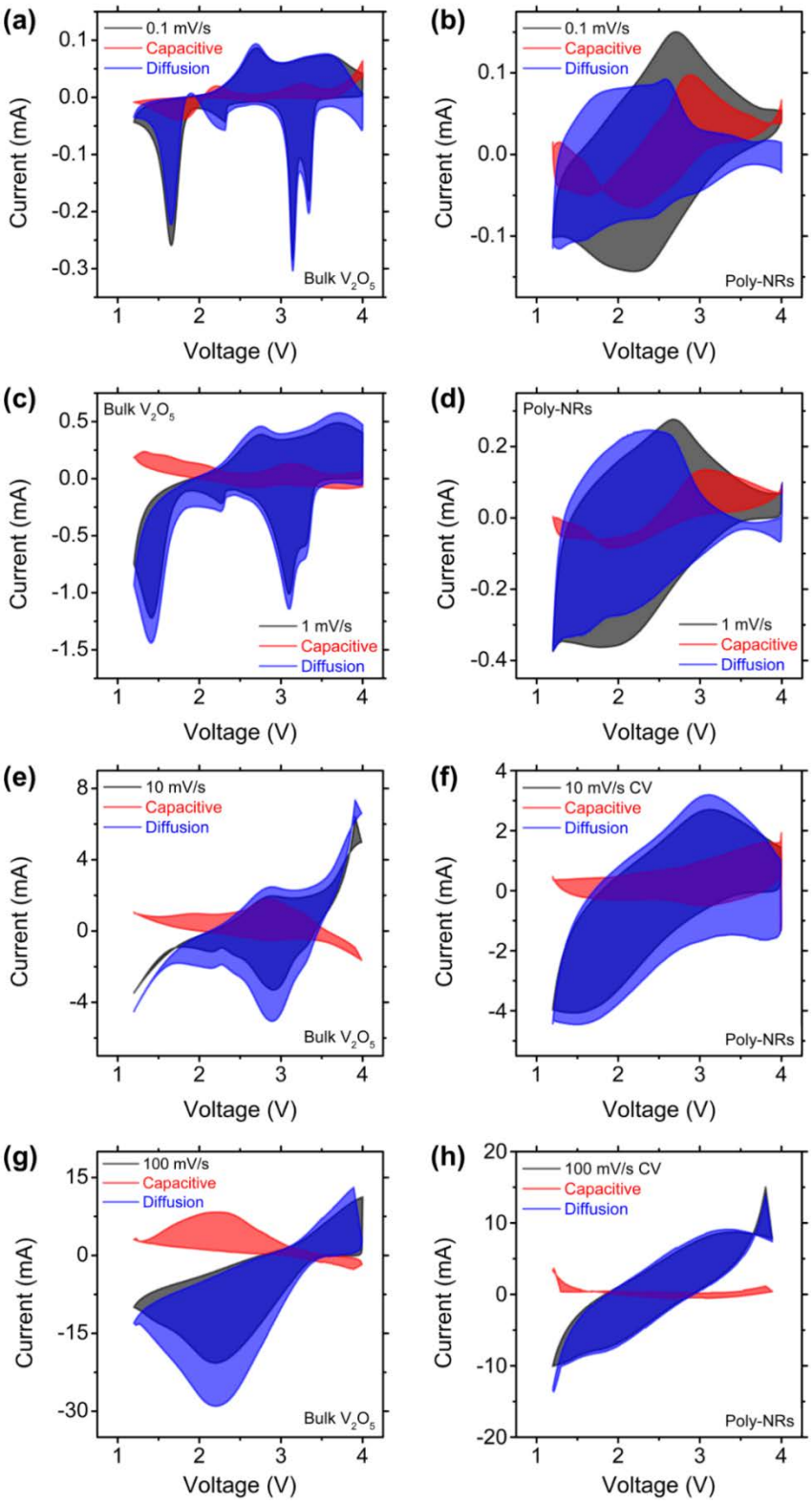

Figure 6. Intercalation (blue) and capacitive (red) contributions to the total measured current (black) for bulk V_2O_5 and poly-NRs at scans rates of 0.1 mV/s (a) and (b), 1 mV/s (c) and (d), 10 mV/s (e) and (f) and 100 mV/s (g) and (h). The capacitance contributions found with opposite polarity of current (or outside the area of the measured current in grey) are a consequence of the deconvolution from the measured current. The sum of indicative

intercalation and capacitive contributions at each potential equals the actual measured current (grey).

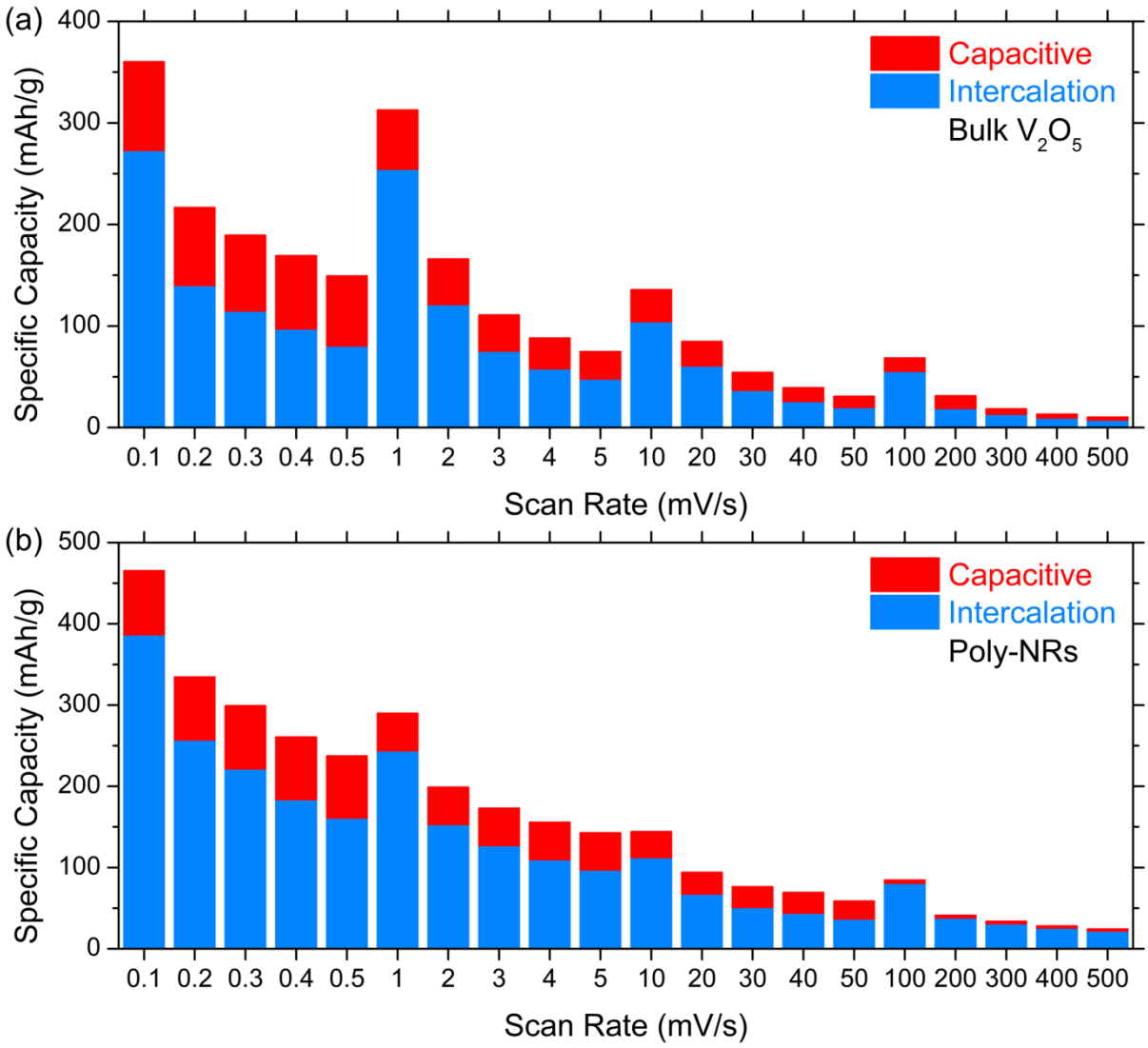

Figure 7. Intercalation (blue) and capacitive (red) contributions to specific capacity for (a) bulk V_2O_5 and (b) poly-NRs. Data were acquired from four cycles in each of four cells using scan rate ranges of 0.1-0.5 mV/s, 1-5 mV/s, 10-50 mV/s and 100-500 mV/s.

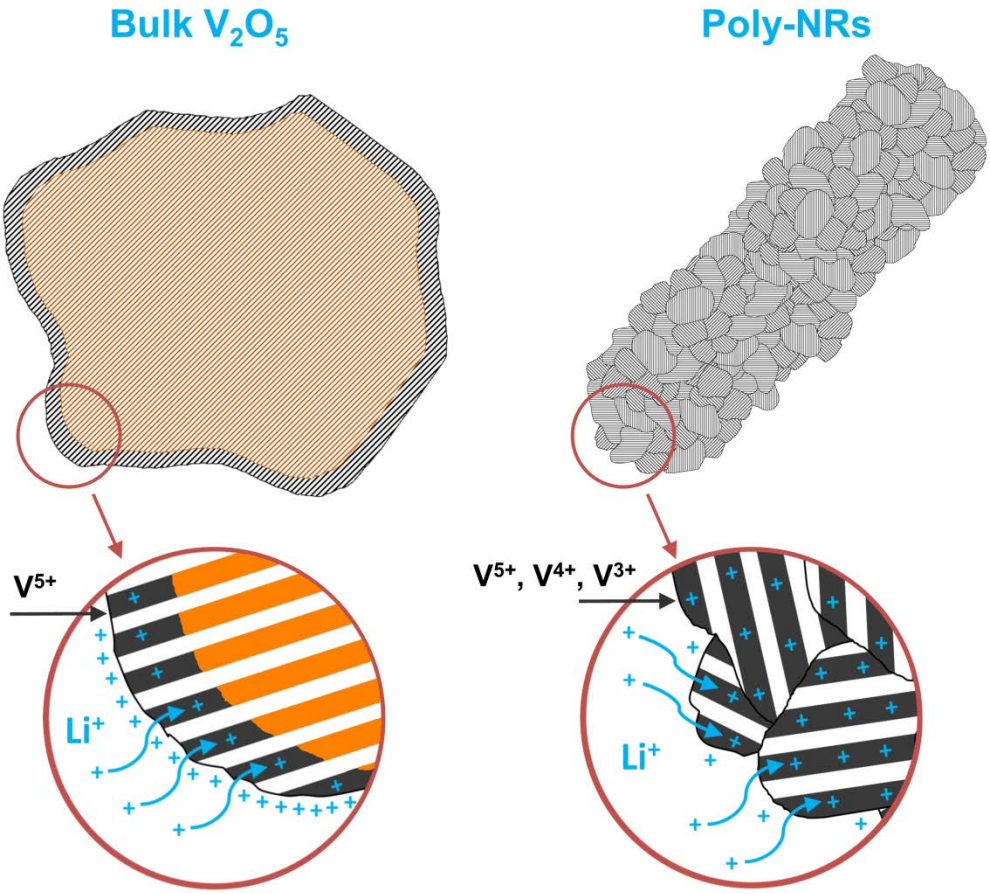

Figure 8. Schematic representation of proposed charge storage mechanisms for bulk V_2O_5 particles and poly-NRs.